Annals of Biomedical Engineering, Vol. 35, No. 7, July 2007 *(© 2007)* pp. 1175–1187
DOI: 10.1007/s10439-007-9287-9

Noninvasive Determination of Ligament Strain with Deformable Image Registration

NIKHIL S. PHATAK,[1] QUNLI SUN,[1] SEONG-EUN KIM,[2] DENNIS L. PARKER,[2] R. KENT SANDERS,[2] ALEXANDER I. VERESS,[1] BENJAMIN J. ELLIS,[1] and JEFFREY A. WEISS [1]

[1]Department of Bioengineering, University of Utah, 50 S. Central Campus Drive, Rm. 2480, Salt Lake City, UT 84112, USA; and [2]Department of Radiology, University of Utah, Salt Lake City, UT 84112, USA

(Received 4 July 2006; accepted 26 February 2007; published online 30 March 2007)

Abstract—Ligament function and propensity for injury are directly related to regional stresses and strains. However, noninvasive techniques for measurement of strain are currently limited. This study validated the use of Hyperelastic Warping, a deformable image registration technique, for noninvasive strain measurement in the human medial collateral ligament using direct comparisons with optical measurements. Hyperelastic Warping determines the deformation map that aligns consecutive images of a deforming material, allowing calculation of strain. Diffeomorphic deformations are ensured by representing the deformable image as a hyperelastic material. Ten cadaveric knees were subjected to six loading scenarios each. Tissue deformation was documented with magnetic resonance imaging (MRI) and video-based experimental measurements. MRI datasets were analyzed using Hyperelastic Warping, representing the medial collateral ligament (MCL) with a hexahedral finite element (FE) model projected to a manually segmented ligament surface. The material behavior was transversely isotropic hyperelastic. Warping predictions of fiber stretch were strongly correlated with experimentally measured strains ($R^2 = 0.81$). Both sets of measurements were in agreement with previous *ex vivo* studies. Warping predictions of fiber stretch were insensitive to bulk:shear modulus ratio, fiber stiffness, and shear modulus in the range of +2.5SD to −1.0SD. Correlations degraded when the shear modulus was decreased to 2.5SD below the mean ($R^2 = 0.56$), and when an isotropic constitutive model was substituted for the transversely isotropic model ($R^2 = 0.65$). MCL strains in the transitional region near the joint line, where the material behavior and material symmetry are more complex, showed the most sensitivity to changes in shear modulus. These results demonstrate that Hyperelastic Warping requires the use of a constitutive model that reflects the material symmetry, but not subject-specific material properties for accurate strain predictions for this application. Hyperelastic Warping represents a powerful technique for noninvasive strain measurement of musculoskeletal tissues and has many advantages over other image-based strain measurement techniques.

Address correspondence to Jeffrey A. Weiss, Department of Bioengineering, University of Utah, 50 S. Central Campus Drive, Rm. 2480, Salt Lake City, UT 84112, USA. Electronic mail: jeff.weiss@utah.edu

Keywords—Strain measurement, Ligament, Deformable image registration, Hyperelastic Warping.

INTRODUCTION

Mechanical stresses and strains within musculoskeletal tissues reflect joint function. Ligaments are complex three-dimensional structures that exhibit highly inhomogeneous strain patterns.[15,21] For example, while collagen within other musculoskeletal tissues may organize with directional isotropy,[14] knee ligaments exhibit a preferred local fiber direction that tends to run the length of the ligament but shows some spatial variability.[49] A spatially inhomogeneous anisotropy is fundamental in describing the specialized function of ligament within a joint, and the structure of a ligament is directly related to the development of regional stresses during applied loads.[36] Ideally, quantification of both *in vivo* stresses and strains may be used to identify normal ligament function and alterations due to injury or disease.[49]

Since *in vivo* noninvasive measurement of ligament stress is currently not possible, experimental investigations have inferred ligament mechanical function through the measurement of strain[1,8,15,23] rather than stress. Techniques that have been used for noninvasive strain measurement in soft tissues include texture correlation[5,6,18] and magnetic resonance (MR) tagging.[33,35,50] Texture correlation requires the presence of well-defined textural details that can be tracked between image pairs and does not provide any constraint to ensure diffeomorphic mappings for large deformations,[34] while MR tagging is limited to loadings that can be repeated cyclically because of the need to tag and then acquire MR data along separate spatial directions sequentially.[33] Historically, even invasive measurement of ligament strain has proven to be challenging because constraints in access and visibility

to the ligament limit the application of traditional optical or strain gauge techniques. Ligament strains have been measured both *in vivo* and *ex vivo* using techniques such as implantation of magnets,[1,8] mercury strain gauges,[23] and optical markers.[15] Due to their intrinsic invasiveness, these methods have been most frequently applied for *ex vivo* studies.

Algorithms for deformable image registration[42,44,47] have become a viable option for ligament strain measurement due to recent advances in MR imaging pulse sequences that enhance the signal intensity of collagen.[9,26] Deformable image registration is used to determine a deformation map that aligns the features of one image with the corresponding features in another image.[44] If these image pairs represent distinct states of deformation, it is possible to determine the strain in the tissue from the deformation map that aligns the image datasets. Deformable image registration is typically an ill-posed problem[20] because a unique solution for the alignment of the two sets of images does not exist. Therefore, a regularization and/or cost function must be used. Our laboratory has developed and applied Hyperelastic Warping,[38,42,43,47] a specific algorithm for deformable image registration, to measure strain directly from medical image data. Hyperelastic Warping combines an image-based energy calculated from the intensity fields of the image pairs with a hyperelastic regularization of the underlying deformation field. An initial template image is chosen to represent the material in the reference configuration, while a target image is chosen to represent the same material after deformation. A spatially varying force is produced to deform the discretized template image into the target image by minimizing an energy functional. Since it is based strictly on image data, strain measurement with Hyperelastic Warping can be noninvasive.

The purpose of this study was to validate the use of Hyperelastic Warping for noninvasive measurement of ligament strain by direct comparison of strains predicted by Warping to experimental optical strain measurements. The sensitivity of Hyperelastic Warping predictions to errors in material model selection and material coefficients was determined. The medial collateral ligament (MCL) was selected for study due to extensive data in the literature on MCL strain behavior,[1,15,23] the availability of validated experimental protocols for ligament strain measurement,[27] high-resolution MR image data is available,[26] and ligament mechanical function is pivotal for knee injury and healing.[49] Two hypotheses were tested: (1) Hyperelastic Warping can accurately predict MCL fiber stretch (final length/initial length along the local fiber direction) during passive knee flexion and knee flexion with valgus torque and (2) variations in the assumed material coefficients and constitutive model have a minimal effect on the predicted fiber stretch distributions.

MATERIALS AND METHODS

Study Design

Ten fresh-frozen, cadaveric, male, left knees were tested (mean age: 48 years; SD: 14; range: 18–65). A pilot study was performed on an additional knee (male, age 64) in order to optimize the MR acquisition settings and to obtain estimates of means and variance for power analysis. Exclusion criteria were surgical scars or evidence of joint disease such as osteoarthritis. Based on estimates for the means and standard deviations of MCL strain from the pilot study combined with previously published data,[15] a power analysis demonstrated that a sample size of 10 was sufficient to obtain a power of 0.8 when detecting a physiologically relevant effect size set at 1.0% strain change during knee flexion with 12 N m valgus torque. A custom loading fixture was designed to allow application of six distinct loading states to the knees in a magnetic resonance imaging (MRI) scanner. The knee at full extension was defined as the reference configuration for strain measurement, and five different target loading configurations were investigated: 0° flexion with valgus load, 30° passive flexion, 30° flexion with valgus load, 60° passive flexion, and 90° passive flexion.

Specimen Preparation

Knee specimens were prepared for kinematic testing and strain measurement using the protocol of Gardiner *et al.*[16] with the exception that more contrast markers were used to define additional gauge lengths and the patella and anterior joint capsule were kept intact during dissection. A 3×8 grid of black plastic spheres (2.38 mm dia.) was bonded to the fibers of the superficial MCL with cyanoacrylate. These contrast markers formed 21 gauge lengths for strain measurement along the visible fiber direction (Fig. 1b). Each gauge length was approximately 9 mm long. The specimen was wrapped in saline-soaked gauze during all testing and was regularly moistened with 0.9% buffered saline. The MCL was exposed for approximately 4–5 h during testing and no visual evidence of dehydration was observed.

Loading Fixture

A custom MRI-compatible (Nylon) fixture was designed to hold the knee at passive flexion angles of 0°, 30°, 60°, and 90°, and apply a calibrated valgus load at 0° and 30° flexion angles (Fig. 1a). A load/torque cell

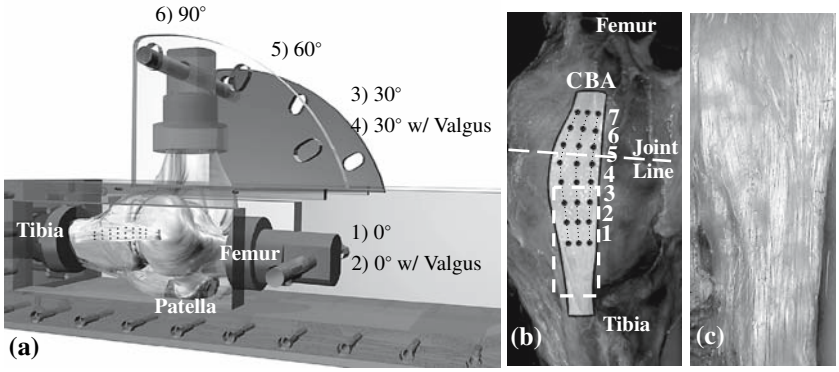

FIGURE 1. (a) Schematic medial view of knee within loading fixture, illustrating the six loading configurations. (1) Initial baseline configuration with 0° flexion (knee at full extension) identified as fiber stretch of 1. (2) 0° flexion with valgus load applied with lateral displacement of proximal femur. (3) 30° passive flexion. (4) 30° flexion with valgus load. (5) 60° passive flexion. (6) 90° passive flexion; (b) Strain measurement locations on the superficial MCL. Anterior strain gauge lengths (Column A) are aligned longitudinally and posterior strain gauge lengths (Column C) are aligned obliquely. Gauge lengths A5, B5, and C5 were positioned across the joint line (dashed line); (c) Photograph depicting fiber direction of distal MCL.

(Futek T5105, Irvine, CA; accuracy ± 0.056 N m) was used for each knee to calibrate the lateral displacement of the distal femur with a valgus torque of 12 N m while tibial motion was constrained in five degrees-of-freedom (only tibial axial rotation permitted). Since the load/torque cell could not be used in the MRI scanner, the calibrated lateral displacement was used to define valgus load. The loading fixture was designed to allow limited but highly repeatable loading conditions, with minor adjustments to accommodate knees of different sizes. The repeatability of knee configurations within the fixture was confirmed for each individual knee with a MicroScribe-3DX digitizer (Immersion Corp., San Jose, CA; accuracy ± 0.085 mm); tracking of anatomic and surface marker landmarks demonstrated that each loading configuration was repeatable to within $\pm 1\%$ error for joint position and flexion angle. The fixture was designed to hold the long axis of the MCL nearly constant with respect to the magnetic field during flexion in order to minimize the effect of directional anisotropy during imaging. The "magic angle effect" creates an artifact of increased signal intensity for collagenous tissue aligned at 55° with respect to the B_0 axis of the MRI scanner.[41] Digitization confirmed that the long axis of the MCL deviated less than 2° with respect to B_0 for all loading conditions, and the magic angle effect was not observed in the resulting MR images. The knee was preconditioned with 15 loading cycles prior to data acquisition at each loading configuration.

Video-based Strain Measurement

Strains were measured from the contrast markers using a 3D motion analysis system consisting of two digital cameras (Pulnix TM-1040, $1024 \times 1024 \times 30$ fps, Sunnyvale, CA) and analysis software (DMAS, Spica Technology Corp, Maui, Hawaii). The accuracy of this system is ± 0.024 mm ($\pm 0.18\%$ absolute strain) for the testing conditions and gauge lengths used in this study.[27] The coordinates of the contrast markers with the knee at full extension were used to define the reference lengths for fiber stretch calculations.

MRI Acquisition and Processing

Several methods were combined to overcome the challenge of obtaining sufficient signal intensity from the MCL with MRI. The T_2 relaxation time constant of collagenous tissue such as ligament has been estimated to be lower than 2 ms.[22] A short echo time (TE), dual echo Spoiled Gradient (SPGR) pulse sequence was developed to obtain signal from the MCL.[17,26] Dual echo images ($TE_1 = 1.6$ ms, $TE_2 = 8.6$ ms, matrix $= 512 \times 256$, field of view $= 16$ cm, slice thickness $= 0.8$ mm) were acquired on a 1.5 T clinical MR scanner (GE Medical Systems, Milwaukee, WI). Two 3-in. diameter, phased-array surface coils were positioned on either side of the knee. To correct for intensity inhomogeneity of the MR data, a bias correction algorithm based on Sled *et al.*[39] was applied separately for each echo. The dual echoes were processed to enhance MCL signal using

$$T_2 \text{ processed signal} = \frac{k}{\ln(echo2/echo1)}, \qquad (1)$$

where $echo1$ and $echo2$ represent the signal intensity of each echo and k is a scaling factor. The MCL was visible at the lower echo time (Fig. 2a, arrows) but not at the higher echo time (Fig. 2b, no arrows).

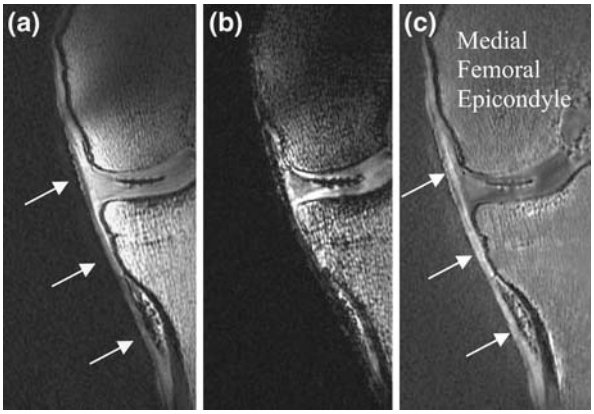

FIGURE 2. Sample coronal slice from a dual-echo MR acquisition of the medial knee. (a) Echo 1, TE_1 = 1.6 ms with MCL clearly visible (white arrows); (b) Echo 2, TE_2 = 8.6 ms with most MCL components not visible; (c) Bias corrected and T_2 processed image used as the basis for Hyperelastic Warping analysis.

Template and Target Images

Image datasets of the MCL were acquired with each knee at 0° passive flexion. These were defined as the template images and represented the reference configuration for each knee. Target image datasets documented the five knee loading configurations for each knee: 0° flexion with valgus load, 30° passive flexion, 30° flexion with valgus load, 60° passive flexion, and 90° passive flexion. Acquisition of each image dataset for this study required approximately 12 min of scan time.

Surface Reconstruction and FE Mesh Generation

The MCL surface was manually segmented from the MR images. Cross-sectional contours of the MCL were extracted from the MRI dataset (SurfDriver, Kailua, HI). The aim of the segmentation process was to create a finite element (FE) mesh that corresponded to the boundary and volume of the MCL (Fig. 3a) to confine the computational solution to the structure of interest. A triangulated MCL surface (Fig. 3b) was imported into FE preprocessing software (TrueGrid, XYZ Scientific, Livermore, CA) and a hexahedral FE mesh was created (Fig. 3c).[13,16]

Finite Deformation Theory

Hyperelastic Warping uses a Lagrangian reference frame to track deformation of the template image. The deformation map that aligns the template image with the target image is denoted $\boldsymbol{\varphi}(\boldsymbol{X}) := \boldsymbol{x} = \boldsymbol{X} + \boldsymbol{u}(\boldsymbol{X})$, where $\boldsymbol{x}$ are current (deformed) coordinates corresponding to $\boldsymbol{X}$ and $\boldsymbol{u}(\boldsymbol{X})$ is the displacement field. The deformation gradient $\boldsymbol{F}$ is defined as

$$\boldsymbol{F}(\boldsymbol{X}) := \frac{\partial \boldsymbol{\varphi}(\boldsymbol{X})}{\partial \boldsymbol{X}}. \tag{2}$$

The change in density is related to $\boldsymbol{F}$ through the Jacobian, $J := \det(\boldsymbol{F}) = \rho_0/\rho$, where ρ_0 and ρ are densities in the reference and deformed configurations, respectively. The positive definite, symmetric right Cauchy–Green deformation tensor is $\boldsymbol{C} = \boldsymbol{F}^{\mathrm{T}}\boldsymbol{F}$.

Hyperelastic Warping

An overview of Hyperelastic Warping is provided below—the details can be found in our previous publications.[38,42–44,47] Most deformable image registration methods can be posed as the minimization of a two-term energy functional with an image-based energy and a regularization/constraint energy.[44] In the following presentation, the spatially varying scalar intensity fields for the template and target are denoted by T and S,

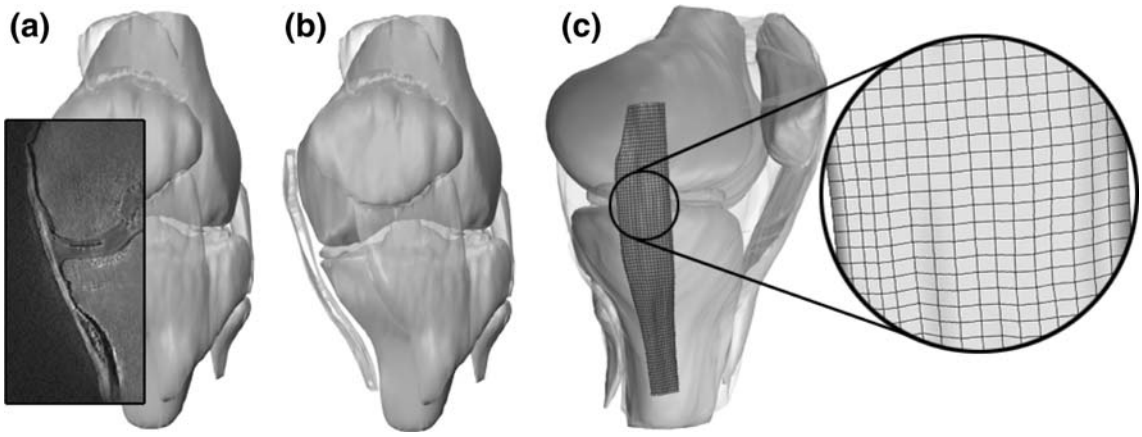

FIGURE 3. Schematic showing the procedure for mesh generation from the MR images. (a) Anterior view of the knee, showing MCL in a coronal slice; (b) Anterior view of triangulated surface, reconstructed from closed bounded contours; (c) Medial view of finite element mesh of MCL with enlargement to show mesh detail.

respectively. For Hyperelastic Warping, the two terms of the energy functional E are defined as[43]

$$E(\boldsymbol{\varphi}) = \int_{\beta} W(\boldsymbol{X}, \boldsymbol{C}) dv - \int_{\beta} U(T(\boldsymbol{X}), S(\boldsymbol{\varphi})) dv. \quad (3)$$

Here, β is the volume of integration in the deformed configuration, W represents the regularization energy, and U is the image-based energy. Hyperelastic Warping takes W to be the strain energy for a hyperelastic material, governed by nonlinear continuum mechanics. Since W depends on $\boldsymbol{C}$, which is independent of rotation, hyperelasticity provides an objective (invariant under rotation) constitutive framework for deformable image registration.[40] The image-based energy used in this study is based on a Gaussian sensor model[10,12,32,43]:

$$U(T(\boldsymbol{X}), S(\boldsymbol{\varphi})) = \frac{\lambda}{2}(T(\boldsymbol{X}) - S(\boldsymbol{\varphi}))^2. \quad (4)$$

Here, λ is a penalty parameter that enforces alignment of the template model with the target image data. As $\lambda \rightarrow \infty$, $(T(\boldsymbol{X}) - S(\boldsymbol{\varphi}))^2 \rightarrow 0$, and the image energy converges to a finite, minimized value. The first variation of the functional U in (4) gives rise to the image-based force term:

$$DU(\boldsymbol{X}, \boldsymbol{\varphi}) \cdot \boldsymbol{\eta} = -\lambda \left[(T(\boldsymbol{X}) - S(\boldsymbol{\varphi})) \frac{\partial S(\boldsymbol{\varphi})}{\partial \boldsymbol{\varphi}} \cdot \boldsymbol{\eta} \right]. \quad (5)$$

This vector term drives the template deformation based on pointwise differences in image intensity and the gradient of the target intensity, evaluated at material points in the template model. The first variation of the energy functional $E(\boldsymbol{\varphi})$ in (3) with respect to the deformation $\boldsymbol{\varphi}(\boldsymbol{X})$ in direction $\boldsymbol{\eta}$ gives rise to the Euler–Lagrange equations[32,43]:

$$\begin{aligned} G(\boldsymbol{\varphi}, \boldsymbol{\eta}) := & DE(\boldsymbol{\varphi}) \cdot \boldsymbol{\eta} = \int_{\beta} \boldsymbol{\sigma} : \nabla \boldsymbol{\eta} \, dv \\ & - \int_{\beta} \lambda \left[(T - S) \frac{\partial S}{\partial \boldsymbol{\varphi}} \cdot \boldsymbol{\eta} \right] dv = 0, \end{aligned} \quad (6)$$

where $\boldsymbol{\sigma}$ is the second-order symmetric Cauchy stress tensor,

$$\boldsymbol{\sigma} = \frac{1}{J} \boldsymbol{F} \frac{\partial W}{\partial \boldsymbol{C}} \boldsymbol{F}^{\mathrm{T}}. \quad (7)$$

The first term on the right-hand side of (6) represents the weak form of the equilibrium equations from continuum mechanics (see, e.g., Marsden and Hughes[30]). The second term is the image-based force term, which drives the deformation of the template model. The image-based forces deform the discretized template model into registration with the target image dataset. They are opposed by the internal forces arising from the deformation of the template image, governed by the form of the hyperelastic strain energy.

Finite Element Discretization

The Hyperelastic Warping algorithm has been integrated into the nonlinear finite element code NIKE3D.[29] The template image data T are interpolated to the nodes of the hexahedral FE mesh to represent part or all of the template image domain. As the mesh deforms, the target image data S are queried at the current location of nodes in the template FE mesh. After linearization of Eq. (6) about a known configuration $\boldsymbol{\varphi}^*$, FE discretization and global assembly, the assembled FE mesh is represented by a system of linear equations:

$$\sum^{e} \left(\boldsymbol{K}^{\mathrm{C}}(\boldsymbol{\varphi}^*) + \boldsymbol{K}^{\mathrm{I}}(\boldsymbol{\varphi}^*) \right) \cdot \Delta \boldsymbol{u} = \sum^{e} \left(\boldsymbol{F}^{\mathrm{ext}}(\boldsymbol{\varphi}^*) + \boldsymbol{F}^{\mathrm{int}}(\boldsymbol{\varphi}^*) \right), \quad (8)$$

where $\sum^{e}$ is the FE assembly operator, assembling contributions from all nodes/elements into the global matrices/vectors. $\boldsymbol{F}^{\mathrm{ext}}$ is the external force vector arising from the image-based energy, $\boldsymbol{F}^{\mathrm{int}}$ is the internal force vector arising from the hyperelastic strain energy, $\boldsymbol{K}^{\mathrm{C}}$ is the constraint stiffness arising from the hyperelastic energy and $\boldsymbol{K}^{\mathrm{I}}$ is the image-based stiffness. The term in parentheses on the left-hand side is the (symmetric) tangent stiffness matrix. $\Delta \boldsymbol{u}$ is the vector of unknown incremental nodal displacements with length $[3 \times N_{\mathrm{el}}]$, where N_{el} is the number of elements. An initial estimate of $\Delta \boldsymbol{u}$ is obtained by inverting Eq. (8), and this solution is improved iteratively using the BFGS quasi-Newton method.[31] The solution is evolved in computational time by incrementally increasing the penalty parameter λ.[44] For this study, the stopping criterion for ending the incremental-iterative solution scheme was defined by a maximum change in the norm of the difference image of less than 5%.

Constitutive Model

When applied to strain tracking problems, Hyperelastic Warping has an advantage over other deformable image registration techniques in that the regularization/constraint can be based on the actual physical material behavior of the structure or tissue of interest. The MCL has a predominant collagen fiber orientation aligned with the longitudinal direction. The material symmetry can be described by a transversely isotropic hyperelastic model, with longitudinal collagen fibers embedded in an isotropic matrix.[13,16,37] A

transversely isotropic hyperelastic strain energy was used, the preferred direction aligned with the long axis of the MCL:

$$W = C_1(\tilde{I}_1 - 3) + F_2(\tilde{\lambda}) + \frac{K}{2}[\ln(J)]^2. \quad (9)$$

$\tilde{I}_1$ is the first deviatoric invariant of $\boldsymbol{C}$,[40] $\tilde{\lambda} = \sqrt{\boldsymbol{a}_0 \cdot \tilde{\boldsymbol{C}} \cdot \boldsymbol{a}_0}$ is the deviatoric fiber stretch along the local fiber direction $\boldsymbol{a}_0$, C_1 is the shear modulus of the matrix and K is the bulk modulus. The fiber stress–stretch behavior was represented as exponential, with no resistance to compressive load:

$$\begin{aligned} \tilde{\lambda}\frac{\partial F_2}{\partial \tilde{\lambda}} &= 0, & \tilde{\lambda} \le 1, \\ \tilde{\lambda}\frac{\partial F_2}{\partial \tilde{\lambda}} &= C_3\left[\exp\left(C_4\left(\tilde{\lambda} - 1\right)\right) - 1\right], & 1 < \tilde{\lambda} < \lambda^*, \\ \tilde{\lambda}\frac{\partial F_2}{\partial \tilde{\lambda}} &= C_5\tilde{\lambda} + C_6, & \tilde{\lambda} \ge \lambda^*. \end{aligned} \quad (10)$$

Here, λ^* is the stretch at which collagen is straightened, C_3 scales the stresses, C_4 defines the fiber uncrimping rate, C_5 is the modulus of straightened collagen fibers, and C_6 was determined from the condition that the collagen stress is C^0 continuous at λ^*. A description of the constitutive model and its FE implementation can be found in our previous publications.[16,46] The following material coefficients were used for the MCL, as reported by Gardiner *et al.*[16]: C_1 = 1.44 MPa, C_3 = 0.57 MPa, C_4 = 48.0 (no units), C_5 = 467 MPa. While the value of the bulk modulus has not been experimentally determined for any ligament, it was assumed to define a nearly incompressible material as two orders of magnitude greater than the shear modulus C_1. This is consistent with the approach used in our previous FE studies of MCL mechanics.[13,16,48]

Spatial Filtering

The solution approach described above follows the local gradient to search for a minimum in the total energy $E(\boldsymbol{\varphi})$ and therefore it is susceptible to local minima. It is often possible to avoid local minima and converge to a global minimum by first registering larger image features, such as object boundaries and coarse textural detail, followed by registration of fine detail. Sequential low-pass spatial filtering was used to achieve this goal.[19,44] By evolving the cut-off frequency of the spatial filter over computational time, the influence of fine textural features in the image can be initially suppressed until global registration is achieved. The spatial filter is applied by convolution of the template and target images with a kernel $\kappa(\boldsymbol{X})$. For the template image,

$$T^*(\boldsymbol{X}) = T(\boldsymbol{X}) * \boldsymbol{\kappa}(\boldsymbol{X}) = \int_B T(\boldsymbol{Z})\boldsymbol{\kappa}(\boldsymbol{X} - \boldsymbol{Z})d\boldsymbol{Z}, \quad (11)$$

where $T(\boldsymbol{X})$ and $T^*(\boldsymbol{X})$ are the original and filtered template image data, respectively, in the spatial domain, $\boldsymbol{X}$ is a vector containing the material coordinates and $\boldsymbol{Z}$ is the frequency representation of $\boldsymbol{X}$. This calculation was performed using the discrete Fourier transform.

Computational Models of the MCL

Each FE model initially consisted of approximately 9000 nodes and 6500 elements. A mesh convergence study was performed on a representative model. The FE models of the MCL were analyzed on four processors of an SGI Origin 3800 (IP35 processors) and required approximately 20 min of wall clock time.

Sensitivity Studies

While the Warping solution is driven by the image data as a "hard constraint", the hyperelastic constitutive model acts as a "soft constraint", ensuring that the deformation field $\boldsymbol{\varphi}(\boldsymbol{X})$ is diffeomorphic and physically representative of the material of interest. To investigate the sensitivity of the Hyperelastic Warping predictions to changes in material coefficients, the material coefficients were varied in the following manner for one randomly chosen model: Coefficient $C_1 \pm 1$ standard deviation (SD) and $\pm$2.5SD with all other properties unchanged; ratio of bulk:shear modulus by $\pm$factor of 10 with all other properties unchanged; fiber stiffness varied by $\pm$30% by adjusting C_3 and C_5 with the following equations:

$$C_5' = 1.3 \times C_5 \quad (12)$$

$$C_3' = C_5' \times \left(\frac{C_3}{C_5}\right) \quad (13)$$

The standard deviations were taken from Gardiner *et al.*[16] In addition, an isotropic constitutive model was assumed to investigate the effect of material symmetry on predictions of fiber stretch by Hyperelastic Warping.

Statistical Analysis

Regression analyses were used to evaluate the ability of Hyperelastic Warping to predict experimental values of MCL fiber stretch. Fiber stretch values for the

deformed FE models were extracted at the locations of the pre-determined gauge lengths as defined by the three-dimensional position of the optical strain markers on the MCL. FE values were averaged over the gauge lengths for comparison with experimental values. The predicted stretches were calculated and tabulated for all knees and compared to experimental results. Coefficients of determination (R^2), regression lines, and p-values were determined. Significance was determined at $p = 0.05$.

RESULTS

A mesh convergence study determined that a minimum of 5500 elements was required for the MCL warping analyses. This FE mesh was approximately 60 elements long, 15 elements wide and 4 elements thick corresponding to an average element size of 1.5 mm (length) × 0.75 mm (width) × 0.5 mm (thickness) (Figs. 3c and 4). Further mesh refinement resulted in fiber stretch predictions that were less than 1% different than those using the 5500 element mesh.

Hyperelastic Warping predictions of regional fiber stretch were strongly correlated with experimental measurements. A regression line for the best fit of all data (21 gauge lengths for 10 knees) yielded a coefficient of regression of $R^2 = 0.81$ ($p = 0.011$, Fig. 5). The root-mean-squared error between the experimental fiber stretch measurements and the Warping predicted values was 1.0091 in units of fiber stretch, or 0.91% fiber strain. Coefficients of determination for each loading configuration were as follows: $R^2 = 0.81$ for 30° passive knee flexion ($p = 0.020$); $R^2 = 0.87$ for 60° passive knee flexion ($p = 0.008$); $R^2 = 0.76$ for 90° passive knee flexion ($p = 0.013$); $R^2 = 0.78$ for 0° flexion with 12 N m valgus load ($p = 0.028$); and $R^2 = 0.86$ for 30° flexion with 12 N m valgus load ($p = 0.007$).

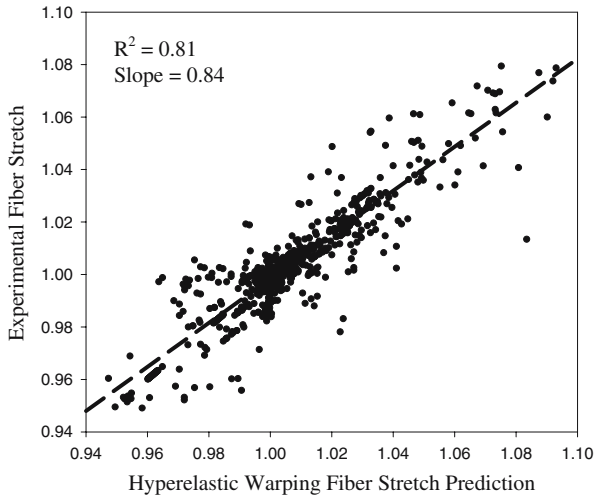

FIGURE 5. Correlation plot of all fiber stretch predictions from Hyperelastic Warping versus experimental fiber stretch measurements indicate that the Warping predictions exhibit strong correlation with experimental strain results. Data are for 21 gauge lengths for five loading configurations with 10 knees ($n = 1050$).

FIGURE 4. Hyperelastic Warping solution for knee 1, showing side view of the original and deformed FE mesh superimposed on volumetric MR images of the template and target, respectively. (a) Template with knee at 0° flexion; (b) Deformed template for knee at 30° flexion with 12 N m valgus torque.

MCL Strain Patterns

Experimentally measured and Warping-predicted MCL strains were highly inhomogeneous (Fig. 6). It is important to note that negative strain values do not necessarily represent compression since the reference configuration was defined with a pre-stretched MCL (knee at full extension) and was not a stress-free state. During passive knee flexion from 0° to 90°, fiber stretch ranged from 0.97 to 1.05 (Figs. 6a–6c). With 12 N m valgus torque for flexion up to 30°, fiber stretch ranged from 0.96 to 1.05 (Figs. 6d and 6e). Buckling of the fibers of the posterior, proximal MCL was observed with knee flexion angles of 60° and higher, and these regions are depicted in purple and marked with an asterisk in Figs. 6b and 6c to note that strain trends in this location should be interpreted with caution. The highest strains were located in the proximal, anterior region of the MCL. MCL strain patterns showed similar values and trends as previous data reported in the literature.[1,15,23]

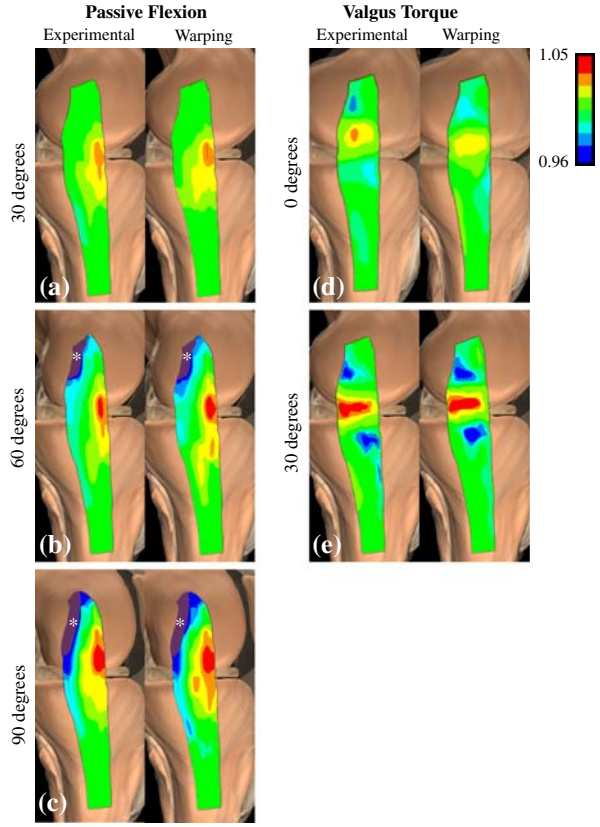

FIGURE 6. The fiber distributions predicted by Hyperelastic Warping show excellent agreement with the experimental strain distributions. Average MCL fiber stretch distributions across all knees (n = 10). (a) 30° passive flexion; (b) 60° passive flexion; (c) 90° passive flexion; (d) 12 N m valgus torque at 0° flexion; (e) 12 N m valgus torque at 30° flexion, experimental (left) and Hyperelastic Warping (right). Discrete values have been interpolated onto the FE mesh to generate a continuous spatial representation of results. (*) Purple regions represent buckling of the posterior, proximal MCL after 60° flexion.

Sensitivity Studies

Hyperelastic Warping predictions of MCL fiber stretch were insensitive to changes in material coefficients for fiber stiffness and bulk modulus:shear modulus ratio. Varying C_1 by ±1SD, bulk:shear ratio by ± factor of 10, and stiffness by ±30% resulted in a negligible change to the overall correlation for all five loading conditions of one knee (Table 1). The effect of variation in C_1 on fiber stretch at specific regions of MCL was charted for ±1SD and ±2.5SD for one randomly chosen computational model and loading condition (Fig. 7). The baseline coefficient of determination for this loading condition was 0.85. Changes in C_1 from +2.5SD down to −1SD did not result in a significant change for correlation. However, the case with C_1 − 2.5SD resulted in a solution with a significantly lower correlation (R^2 = 0.67) with 12 out of 21 strain regions exhibiting limited convergence in comparison to the baseline solution. Strain regions located in the central MCL near the joint line (locations B4, B5, B6) showed the most sensitivity to change in C_1. Overall R^2 for all five loading conditions was 0.78. Correlation was degraded for C_1 − 2.5SD (R^2 = 0.56) and the substitution of an isotropic constitutive model (R^2 = 0.65).

DISCUSSION

This study demonstrated the feasibility of measuring ligament strain using Hyperelastic Warping with volumetric MR images before and after deformation. The use of a hyperelastic strain energy ensures that deformations will be diffeomorphic (one-to-one, onto, and differentiable with a differentiable inverse). Further, hyperelasticity is objective for large strains and rotations and provides a reasonable description of the material behavior of many soft tissues. These characteristics are considered to be major strengths of the method. Previous uses of solid mechanics-based regularizations for deformable image registration have been based on linear elasticity,[2] which is not objective and penalizes large strains and rotations. The use of a

TABLE 1. Effect of variation of material coefficients on Hyperelastic Warping predictions of fiber stretch as represented by the coefficient of determination (R^2) between experimental measurements and Hyperelastic Warping predictions.

	R^2 (30°)	R^2 (60°)	R^2 (90°)	R^2 (0° with valgus load)	R^2 (30° with valgus load)
Baseline Warping	0.79*	0.84*	0.70*	0.74*	0.85*
C_1 + 2.5SD	0.72*	0.81*	0.68*	0.70*	0.79*
C_1 + 1SD	0.79*	0.84*	0.70*	0.74*	0.85*
C_1 − 1SD	0.79*	0.84*	0.70*	0.74*	0.85*
C_1 − 2.5SD	0.63*	0.62	0.51	0.43	0.67
Bulk:shear ratio × 10	0.79*	0.83*	0.69*	0.73*	0.84*
Bulk:shear ratio/10	0.79*	0.83*	0.68*	0.74*	0.84*
Stiffness + 30%	0.79*	0.84*	0.70*	0.74*	0.85*
Stiffness − 30%	0.79*	0.84*	0.70*	0.74*	0.85*
Isotropic	0.68*	0.75*	0.61	0.52	0.72*

One computational model (knee 3) was randomly selected for the sensitivity studies and correlation results are reported for all five loading conditions. An asterisk indicates a statistically significant correlation.

realistic constitutive model for the MCL ensures that deformation maps reflect the behavior of an elastic material under finite deformation. In regions of the template model that have large intensity gradients, large image-based forces will be generated and the solution will be primarily determined by the image data. In regions that lack image texture or gradients, image-based forces will be smaller or in some cases negligible. In these cases the predicted deformation will be dependent on the hyperelastic regularization (constitutive model). A realistic representation of the material behavior serves to improve predictions in these areas.

Warping predictions of fiber stretch and strain were relatively insensitive to changes in C_1 by $\pm$1SD, $C_1 + 2.5$SD, stiffness by $\pm$30%, or bulk:shear ratio by $\pm$ factor of 10. Correlations were significantly degraded with $C_1 - 2.5$SD and with the substitution of an isotropic constitutive model. The relative insensitivity of the fiber stretch predictions from Hyperelastic Warping to changes in material coefficients is consistent with the results of our previous studies of myocardial strain[43] and coronary arteries.[42] The greatest sensitivity in response to a change in C_1 was seen in strain regions B4, B5, B6 located in the central MCL near the joint line (Fig. 7). This portion of the superficial MCL represents the transition between longitudinal anterior fibers and oblique posterior fibers and it is physically contiguous with the deep MCL, which attaches to the medial meniscus. A possible explanation for the relative sensitivity of the Warping solution to C_1 in this particular area is due to the complexity of the material behavior and material symmetry in this transitional zone. The FE model used in this study accounted for the anterior longitudinal and posterior oblique fibers of the superficial MCL, and assumed this same fiber direction through the depth of the MCL.

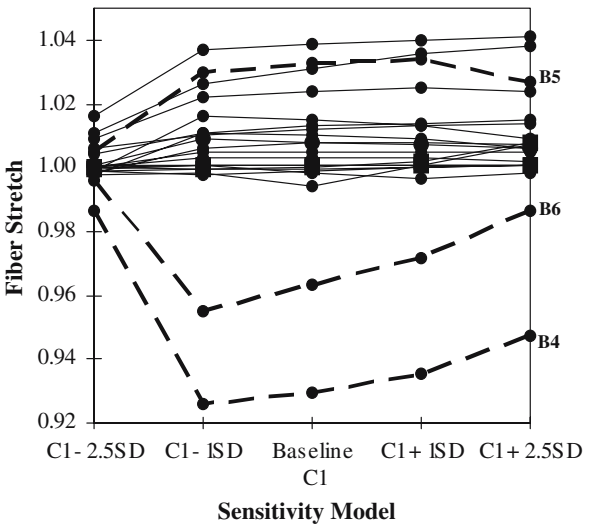

FIGURE 7. Effect of variations in material coefficient C_1 on Hyperelastic Warping fiber stretch predictions for 21 strain regions for one randomly chosen model and loading condition (knee 3, 30° flexion with valgus load). Correlations were significantly degraded at $C_1 - 2.5$SD. Strain regions B4, B5, B6 (dashed lines) showed the greatest sensitivity to change in C_1.

Only superficial MCL strain comparisons were made in this study, and fiber directions were accurately characterized for these locations through visual inspection. Future research with deep MCL strain will require a detailed description of fiber orientation through the thickness of the MCL and its attachments with the medial meniscus, femur, and tibia. This will require the use of histological techniques or possibly diffusion tensor MRI technology.

The results of the sensitivity studies suggest that the use of a constitutive model that represents the general material symmetry of the material improves the accuracy of strain predictions with Hyperelastic Warping. However, the actual values of the material coefficients are not as critical. This is consistent with the fact that changing the shear modulus or ratio of fiber:shear modulus generally had little effect on the quality of the strain predictions by Hyperelastic Warping, whereas the substitution of an isotropic material model for the transversely isotropic model degraded the correlation significantly. The bulk:shear ratio was more insensitive for MCL strain as compared to a previous study with myocardial strain.[43] This could be explained by the fact that compressibility is a more important factor in describing the material constitutive behavior of myocardium, rather than ligament.

Fiber stretch predictions from Hyperelastic Warping and experimental measurements exhibited similar trends in range and spatial location as previous results of MCL strain during passive knee flexion (Table 2). The highest strains in this study occurred in the proximal, anterior region of the MCL. Previous experimental studies[1,15,23] reported that the highest MCL strains occur in the proximal region, and anecdotal clinical evidence suggests that most MCL injuries also occur at the proximal insertion site.[25] Arms *et al.*[1] and Hull *et al.*[23] reported increasing strain for the anterior MCL with increasing flexion angle in the range of 0–4%, and this pattern matches the results in this study. In contrast, Gardiner *et al.*[15] found no difference in strain for the anterior MCL with increased flexion angle, although this differing pattern was likely due to the removal of the patella and anterior capsule. The posterior MCL exhibited decreasing strain with increasing flexion angle in the range of −3 to 0%. These results are in agreement with Arms *et al.*[1] and Gardiner *et al.*[15] In addition, buckling of the proximal, posterior MCL (Figs. 6b, c, purple regions denoted with asterisk) with

TABLE 2. MCL strain changes with increasing knee flexion.

	Arms *et al.*[1]	Hull *et al.*[23]	Gardiner *et al.*[15]	Experimental, present study	Hyperelastic Warping, present study
Technique	Hall device	Mercury strain gauges	3D motion analysis	3D motion analysis	Deformable image registration
Reference configuration	0 degree flexion	Inflection point on load/strain curve	*In situ* (dissected ligament)[a]	0° flexion	0° flexion
Location of highest strain	Proximal anterior MCL	Proximal anterior MCL	Proximal posterior MCL	Proximal anterior MCL	Proximal anterior MCL
Anterior strain—passive flexion to 90°	0 to 4%	–	–1 to 1%[a] (anterior capsule removed)	0 to 5%	0 to 5%
Posterior strain—passive flexion to 90°	–4 to 0%	–	–5 to 0%[a]	–3 to 0%	–3 to 0%
Anterior strain—valgus load up to 30°	0 to 3% (15 N m torque)	1 to 2%	0 to 2%[a] (10 N m torque)	0 to 3% (12 N m torque)	–1 to 3% (12 N m torque)
Posterior strain—valgus load up to 30°	0 to 4% (15 N m torque)	–	–1 to 4%[a] (10 N m torque)	–4 to 5% (12 N m torque)	–4 to 5% (12 N m torque)

Comparison with previous studies. Strains with respect to 0° flexion.
[a]Data for Gardiner *et al.* were adjusted from *in situ* values.

knee flexion angles greater than 60° exhibited similar patterns as Gardiner *et al.*[15]

The accuracy of strain predictions using Hyperelastic Warping depends on the resolution and textural detail of the image data, and its application requires loading scenarios that allow high-resolution imaging both before and after the deformation. We performed extensive optimization of MR acquisition parameters to achieve high-resolution images of the MCL while optimizing signal-to-noise ratio. A short TE pulse sequence was critical for MR imaging of the MCL due to rapid decay of MR signal in collagen containing ligaments.[17] In addition, dual echo images[9] were used to refine the boundaries of the MCL. To increase textural detail through the MCL thickness, a nonuniform acquisition matrix was used with twice the image resolution in the MCL thickness direction as compared to the MCL length direction. The dataset was then resampled with interpolation to create homogeneous-sized voxels.

The loading configurations for this study were partially dictated by the geometry of the MRI scanner. The size of the bore and the need for an MRI-compatible loading fixture restricted the range of motion and the forces that could be applied. In the future, open MR scanners and shorter acquisition times will enable the application of more clinically relevant loading scenarios and the ability to perform *in vivo* musculoskeletal strain measurement. While *ex vivo* studies of ligament strain have elucidated ligament mechanical function, *in vivo* measurements will allow the investigation of ligament strains during muscle activation and weightbearing. In addition, since knee ligaments are often injured in combination, *in vivo* analysis may aid in the differential diagnosis and localization of ligament injury. Injured joints could be analyzed for functional performance based on strain values throughout the joint, isolating partial injuries which could not be otherwise located.

In addition to Hyperelastic Warping, both texture correlation and MR tagging have been used for image-based strain measurement. Texture correlation has been applied successfully for the measurement of a variety of musculoskeletal tissue strains including bone,[4,5,34] cartilage,[18,45] and tendon.[6,7] A signal intensity pattern surrounding each pixel is used to track pixel displacement between images. Since only an image-based energy term is used in the texture correlation algorithm,[18] the technique is relatively sensitive to noise. Practical implementation for strain measurement requires manual alignment of images to account for rigid body rotation.[34] For Hyperelastic Warping, the constitutive model is unaffected by rigid body rotations by design. A limitation of Hyperelastic Warping is that the computational expense associated with solving the

equations emanating from the combined energy functional is considerably higher than that associated with analyses based on texture correlation.

MR tagging has been primarily used as a noninvasive, image-based method for measuring myocardial strain.[35,50] MR tagging relies on local perturbation of the magnetization of the myocardium with selective radio-frequency saturation to produce multiple, thin tag planes. The resulting magnetization lines are used as fiducials to track the deformation of the myocardium. Two to three orthogonal tag sets must be acquired to determine 3D deformation. Recently, MR tagging has been adapted for musculoskeletal applications. Neu *et al*.[33] examined articular cartilage strain using the specialized MRI tagging technique "*delays alternating with nutations for tailored excitation*" (DANTE) with high density tag lines. A primary limitation of MR tagging is that images must be acquired over repeated cycles. While cyclic loading is achieved *in vivo* for the beating myocardium, an external, cyclic loading device is required for musculoskeletal applications.[33]

Deformable image registration models that use regularizations based on the constitutive behavior of linear elastic materials and fluids have been used extensively in the field of anatomical brain registration. Measures of image similarity take the form of differences in the square of the image intensities[10–12,24,38,47] or are based on cross-correlation methods of the intensity or intensity gradient values.[28] When the regularization term of the energy functional is derived from the constitutive model, the registration process takes on the characteristics of the underlying material model. For example, registration methods that use a viscous or inviscid fluid constitutive model have been shown to provide excellent registration results.[10,11] However, these models have a tendency to underpenalize shear deformations and thus produce physically unrealistic registration of solids. In other words, the deformation of the deformable template resembles that of a fluid rather than that of a solid. Other continuum based methods for deformable image registration use linear elasticity to regularize registration.[2,3,10,11] The use of linear elasticity is attractive due to the fact that it is relatively simple to implement. However, it has a tendency to over-penalize large deformations involved in inter- or intra-subject registration. This is due to the fact that linear elasticity is not objective (rotationally invariant). As a result, even the smallest rotation of material axes induces stress in a linear elastic solid.

In conclusion, this study developed a high-resolution MR imaging strategy for the human MCL and demonstrated that when the resulting image data were used with Hyperelastic Warping, accurate predictions of the magnitudes and spatial variations of ligament strain were possible. The material coefficient/model sensitivity studies demonstrated that strain predictions were relatively insensitive to material coefficients associated with the hyperelastic regularization. Hyperelastic Warping represents a powerful technique for noncontact strain measurement in musculoskeletal soft tissues, and it shows promise for application to noninvasive measurement of soft tissue strain *in vivo*.

ACKNOWLEDGMENTS

Financial support from NSF #BES-0134503 is gratefully acknowledged. The authors thank Garry Gold of Stanford University for suggesting the use of a nonuniform acquisition matrix, and Marianne Bergquist, Jeff McCann and Anita Apte for assistance with experiments and image acquisition.

REFERENCES

[1]Arms, S., J. Boyle, R. Johnson, and M. Pope. Strain measurement in the medial collateral ligament of the human knee: an autopsy study. *J. Biomech.* 16(7):491–496, 1983.

[2]Bajcsy, R., R. Lieberson, and M. Reivich. A computerized system for the elastic matching of deformed radiographic images to idealized atlas images. *J. Comput. Assist. Tomogr.* 7(4):618–625, 1983.

[3]Bajcsy, R., and S. Kovacic. Multiresolution elastic matching. *Comput. Vis. Graphics Image Process* 46:1–21, 1989.

[4]Bay, B. K. Texture correlation: a method for the measurement of detailed strain distributions within trabecular bone. *J. Orthop. Res.* 13(2):258–267, 1995.

[5]Bay, B. K, S. A. Yerby, R. F. McLain, and E. Toh. Measurement of strain distributions within vertebral body sections by texture correlation. *Spine* 24(1):10–17, 1999.

[6]Bey, M. J., H. K. Song, F. W. Wehrli, and L. J. Soslowsky. Intratendinous strain fields of the intact supraspinatus tendon: the effect of glenohumeral joint position and tendon region. *J. Orthop. Res.* 20(4):869–874, 2002.

[7]Bey, M. J., H. K. Song, F. W. Wehrli, and L. J. Soslowsky. A noncontact, nondestructive method for quantifying intratissue deformations and strains. *J. Biomech. Eng.* 124(2):253–258, 2002.

[8]Beynnon, B. D., B. C. Fleming, R. J. Johnson, C. E. Nichols, P. A. Renstrom, and M. H. Pope. Anterior cruciate ligament strain behavior during rehabilitation exercises *in vivo*. *Am. J. Sports Med.* 23(1):24–34, 1995.

[9]Bruder, H., H. Fischer, R. Graumann, and M. Deimling. A new steady-state imaging sequence for simultaneous acquisition of two mr images with clearly different contrasts. *Magn. Reson. Med.* 7(1):35–42, 1988.

[10]Christensen, G. E., R. D. Rabbitt, and M. I. Miller. 3D brain mapping using a deformable neuroanatomy. *Phys. Med. Biol.* 39(3):609–618, 1994.

[11]Christensen, G. E., R. D. Rabbitt, and M. I. Miller. Deformable templates using large deformation kinematics. *IEEE Trans. Image Process.* 5(10):1435–1447, 1996.

[12]Christensen, G. E., and H. J. Johnson. Consistent image registration. *IEEE Trans. Med. Imaging* 20(7):568–582, 2001.
[13]Ellis, B. J., T. J. Lujan, M. S. Dalton, and J. A. Weiss. Medial collateral ligament insertion site and contact forces in the acl-deficient knee. *J. Orthop. Res.* 24(4):800–810, 2006.
[14]Federico, S., A. Grillo, G. La Rosa, G. Giaquinta, and W. Herzog. A transversely isotropic, transversely homogeneous microstructural-statistical model of articular cartilage. *J. Biomech.* 38(10):2008–2018, 2005.
[15]Gardiner, J. C., J. A. Weiss, and T. D. Rosenberg. Strain in the human medial collateral ligament during valgus loading of the knee. *Clin. Orthop.* 391:266–274, 2001.
[16]Gardiner, J. C., and J. A. Weiss. Subject-specific finite element analysis of the human medial collateral ligament during valgus knee loading. *J. Orthop. Res.* 21(6):1098–1106, 2003.
[17]Gatehouse, P. D., and G. M. Bydder. Magnetic resonance imaging of short t2 components in tissue. *Clin. Radiol.* 58(1):1–19, 2003.
[18]Gilchrist, C. L., J. Q. Xia, L. A. Setton, and E. W. Hsu. High-resolution determination of soft tissue deformations using MRI and first-order texture correlation. *IEEE Trans. Med. Imaging* 23(5):546–553, 2004.
[19]Gonzalez, R. C., and R. E. Woods. Digital Image Processing. Addison-Wesley Pub. Co.: Reading, MA, 1992.
[20]Hadamard, J. Sur les problemes aux derivees partielles et leur signification physique. *Bull. Univ. Princeton.* 13, 1902.
[21]Halloran, J. P., A. J. Petrella, and P. J. Rullkoetter. Explicit finite element modeling of total knee replacement mechanics. *J. Biomech.* 38(2):323–331, 2005.
[22]Henkelman, R. M., G. J. Stanisz, J. K. Kim, and M. J. Bronskill. Anisotropy of nmr properties of tissues. *Magn. Reson. Med.* 32(5):592–601, 1994.
[23]Hull, M. L., G. S. Berns, H. Varma, and H. A. Patterson. Strain in the medial collateral ligament of the human knee under single and combined loads. *J. Biomech.* 29(2):199–206, 1996.
[24]Johnson, H. J., and G. E. Christensen. Consistent landmark and intensity-based image registration. *IEEE Trans. Med. Imaging* 21(5):450–461, 2002.
[25]Kawada, T., T. Abe, K. Yamamoto, S. Hirokawa, T. Soejima, N. Tanaka, and A. Inoue. Analysis of strain distribution in the medial collateral ligament using a photoelastic coating method. *Med. Eng. Phys.* 21(5):279–291, 1999.
[26]Kim, S. E., N. Phatak, H. Buswell, E. K. Jeong, J. A. Weiss, and D. L. Parker. Short te double echo 3d spgr acquistion for short t2 imaging. Proceedings of the 11th Scientific Meeting of International Society for Magnetic Resonance in Medicine, Toronto, Canada, 2003.
[27]Lujan, T. J., S. P. Lake, T. A. Plaizier, B. J. Ellis, and J. A. Weiss. Simultaneous measurement of three-dimensional joint kinematics and ligament strains with optical methods. *J. Biomech. Eng.* 127(1):193–197, 2005.
[28]Maintz, J. B., and M. A. Viergever. A survey of medical image registration. *Med. Image. Anal.* 2(1):1–36, 1998.
[29]Maker, B. N., R. M. Ferencz, J. O. Hallquist. Nike3d: a nonlinear, implicit, three-dimensional finite element code for solid and structural mechanics. Lawrence Livermore National Laboratory Technical Report, 1990, UCRL-MA #105268.
[30]Marsden, J. E., and T. J. R. Hughes. Mathematical Foundations of Elasticity. Minneola, NY: Dover, 1994.
[31]Matthies, H., and G. Strang. The solution of nonlinear finite element equations. *Int. J. Numer. Methods Eng.* 14:1613–1626, 1979.
[32]Miller, M. I., A. Trouvé, and L. Younes. On the metrics and euler-lagrange equations of computational anatomy. *Annu. Rev. Biomed. Eng.* 4:375–405, 2002.
[33]Neu, C. P., M. L. Hull, J. H. Walton, and M. H. Buonocore. MRI-based technique for determining nonuniform deformations throughout the volume of articular cartilage explants. *Magn. Reson. Med.* 53(2):321–328, 2005.
[34]Nicolella, D. P., L. F. Bonewald, D. E. Moravits, and J. Lankford. Measurement of microstructural strain in cortical bone. *Eur. J. Morphol.* 42(1–2):23–29, 2005.
[35]O'Dell, W. G., and A. D. McCulloch. Imaging three-dimensional cardiac function. *Annu. Rev. Biomed. Eng.* 2:431–456, 2000.
[36]Provenzano, P. P., D. Heisey, K. Hayashi, R. Lakes, and R. Vanderby Jr. Subfailure damage in ligament: a structural and cellular evaluation. *J. Appl. Physiol.* 92(1):362–371, 2002.
[37]Quapp, K. M., and J. A. Weiss. Material characterization of human medial collateral ligament. *J. Biomech. Eng.* 120(6):757–763, 1998.
[38]Rabbitt, R. D., J. A. Weiss, G. E. Christensen, and M. I. Miller. Mapping of hyperelastic deformable templates using the finite element method. *SPIE* 2573:252–265, 1995.
[39]Sled, J. G., A. P. Zijdenbos, and A. C. Evans. A nonparametric method for automatic correction of intensity nonuniformity in MRI data. *IEEE Trans. Med. Imaging* 17(1):87–97, 1998.
[40]Spencer, A. Continuum Mechanics. New York: Longman, 1980.
[41]Timins, M. E., S. J. Erickson, L. D. Estkowski, G. F. Carrera, and R. A. Komorowski. Increased signal in the normal supraspinatus tendon on mr imaging: diagnostic pitfall caused by the magic-angle effect. *AJR Am. J. Roentgenol.* 165(1):109–114, 1995.
[42]Veress, A. I., J. A. Weiss, G. T. Gullberg, D. G. Vince, and R. D. Rabbitt. Strain measurement in coronary arteries using intravascular ultrasound and deformable images. *J. Biomech. Eng.* 124(6):734–741, 2002.
[43]Veress, A. I., G. T. Gullberg, and J. A. Weiss. Measurement of strain in the left ventricle during diastole with cine-MRI and deformable image registration. *J. Biomech. Eng.* 127(7):1195–1207, 2005.
[44]Veress, A. I., N. Phatak, J. A. Weiss. Deformable image registration with hyperelastic warping. In: Handbook of Biomedical Image Analysis, Vol 3, Registration Models (Part a), edited by J. Suri, D. Wilson, and S. Laxminarayan. New York: Marcel Dekker Inc., 2005, pp. 1–2.
[45]Villemure, I., L. Cloutier, J. R. Matyas, and N. A. Duncan. Non-uniform strain distribution within rat cartilaginous growth plate under uniaxial compression. *J. Biomech.* 40(1):149–156, 2007.
[46]Weiss, J., B. Maker, and S. Govindjee. Finite element implementation of incompressible transversely isotropic hyperelasticity. *Comput. Methods Applic. Mech. Eng.* 135:107–128, 1996.
[47]Weiss, J. A., R. D. Rabbitt, and A. E. Bowden. Incorporation of medical image data in finite element models to track strain in soft tissues. *SPIE* 3254:477–484, 1998.

[48]Weiss, J. A., J. C. Gardiner, B. J. Ellis, T. J. Lujan, and N. S. Phatak. Three-dimensional finite element modeling of ligaments: technical aspects. *Med. Eng. Phys.* 27(10):845–861, 2005.

[49]Woo, S. L., S. D. Abramowitch, R. Kilger, and R. Liang. Biomechanics of knee ligaments: Injury, healing, and repair. *J. Biomech.* 39(1):1–20, 2006.

[50]Zerhouni, E. A., D. M. Parish, W. J. Rogers, A. Yang, and E. P. Shapiro. Human heart: tagging with mr imaging—a method for noninvasive assessment of myocardial motion. *Radiology* 169(1):59–63, 1988.